

Short-wavelength infrared tuneable filters on HgCdTe photoconductors

Martin T. K. Soh*

*Department of Electrical and Computer Engineering, University of Minnesota,
Minneapolis 55455*

**) 2005-6 Fulbright Fellow from CSIRO Industrial Physics and the School of Electrical,
Electronic and Computer Engineering at the University of Western Australia.*

sohxx004@umn.edu

**T. Nguyen, K. K. M. B. D. Silva, R. J. Westerhout,
J. Antoszewski and A. J. Keating**

*School of Electrical, Electronic and Computer Engineering,
The University of Western Australia, Crawley 6009, Australia*

N. Savvides

CSIRO Industrial Physics, Lindfield 2070, Australia

**C. A. Musca,
J. M. Dell and L. Faraone**

*School of Electrical, Electronic and Computer Engineering,
The University of Western Australia, Crawley 6009, Australia*

Abstract: The design, micro-fabrication, and electronic and optical performance of a tuneable short-wavelength infrared Fabry-Pérot resonator on a mercury cadmium telluride photoconductor is presented. The maximum processing temperature of 125 °C has negligible effect on the electronic and optical performance of photoconductor test structures. Maximum responsivity, effective carrier lifetime and detectivity are $60 \times 10^3 \text{ VW}^{-1}$, $2 \times 10^{-5} \text{ s}$ and $8 \times 10^{10} \text{ cmHz}^{1/2}\text{W}^{-1}$, respectively. The maximum effective carrier lifetime and specific detectivity are in good agreement with the theoretical maxima. Uncooled device operation is possible since responsivity is observed not to improve with thermo-electric cooling. Spectral tuning of the micro-filters is demonstrated over the wavelength range 1.7 to 2.2 μm using drive voltages up to 8 V, with the full-width-half-maximum of the resonance approximately 100 nm. Membrane deflection can be up to 40% of the cavity width.

© 2005 Optical Society of America

OCIS codes: (110.3080) Infrared imaging; (040.5150) Photoconductivity; (120.2230) Fabry-Pérot; (310.1860) Deposition and fabrication.

References and links

1. A. Rogalski, "Infrared detectors: status and trends," *Prog. Quantum Electron.* **27**, 59–210 (2003).
2. M. J. Madou, *Fundamentals of Microfabrication: The Science of Miniaturization*, 2nd ed. (CRC Press, 2002).
3. L. J. Kozlowski, G. M. Williams, G. J. Sullivan, C. W. Farley, R. J. Anderson, J. C. D. T. Cheung, W. E. Tennant, and R. E. DeWames, "LWIR 128×128 GaAs/AlGaAs multiple quantum well hybrid focal plane array," *IEEE Trans. Electron Devices* **38**, 1124–30 (1991).
4. G. Sarusi, B. F. Levine, S. J. Pearton, K. M. S. Bandara, and R. E. Leibenguth, "Improved performance of quantum well infrared photodetectors using random scattering optical coupling," *Appl. Phys. Lett.* **64**, 960–2 (1994).

5. R. A. Wood, C. J. Han, and P. W. Kruse, "Integrated uncooled infrared detector imaging arrays," in *Technical Digest. IEEE Solid-State Sensor and Actuator Workshop (Cat. No.92TH0403-X)*, pp. 132–5 (1992).
6. I. H. Choi and K. D. Wise, "A silicon-thermopile-based infrared sensing array for use in automated manufacturing," *IEEE Trans. Electron Devices* **33**, 72–9 (1986).
7. P. G. Datskos, P. I. Oden, T. Thundat, E. A. Wachter, R. J. Warmack, and S. R. Hunter, "Remote infrared radiation detection using piezoresistive microcantilevers," *Appl. Phys. Lett.* **69**, 2986–8 (1996).
8. Y. Zhao, M. Mao, R. Horowitz, A. Majumdar, J. Varesi, P. Norton, and J. Kitching, "Optomechanical uncooled infrared imaging system: design, microfabrication and performance," *J. Microelectromech. Syst.* **11**, 136–46 (2002).
9. C. A. Musca, "Photoconductive infrared detector technology based on epitaxially-grown mercury cadmium telluride heterostructures," Ph.D. thesis, Department of Electrical and Electronic Engineering at The University of Western Australia (1997).
10. M. T. Eismann, C. R. Schwartz, and J. N. C. and R. J. Huppi, "Comparison of infrared imaging hyperspectral sensors for military target detection applications," in *Proc. SPIE – Int. Soc. Opt. Eng.*, vol. 2819, pp. 91–101 (1996).
11. R. W. Basedow, W. S. Aldrich, J. E. Colwell, and W. D. Kinder, "HYDICE system performance – an update," in *Proc. SPIE – Int. Soc. Opt. Eng.*, vol. 2821, pp. 76–84 (1996).
12. C. Simi, E. Winter, M. Williams, and D. Driscoll, "Compact airborne spectral sensor," in *Proc. SPIE – Int. Soc. Opt. Eng.*, vol. 4381, pp. 129–36 (2001).
13. J. Antoszewski, K. J. Winchester, A. J. Keating, T. Nguyen, K. K. M. B. D. Silva, C. A. Musca, J. M. Dell, L. Faraone, P. Mitra, J. D. Beck, M. R. Skokan, and J. E. Robinson, "A monolithically integrated HgCdTe photodetector and Micro-Electro-mechanical Systems-Based optical filter," *J. Electron. Mat.* **34**, 716–21 (2005).
14. M. T. K. Soh, N. Savvides, C. A. Musca, M. P. Martyniuk, and L. Faraone, "Local bonding environment of nitrogen-rich silicon nitride thin films," *J. Appl. Phys.* **97**, 093,714 (2005).
15. M. T. K. Soh, C. A. Musca, N. Savvides, J. M. Dell, and L. Faraone, "Evaluation of plasma deposited silicon nitride thin films for micro-systems-technology," *J. Microelectromech. Syst.* **14**, 971–7 (2005).
16. M. T. K. Soh, A. C. Fischer-Cripps, N. Savvides, C. A. Musca, and L. Faraone, "Nanoindentation of plasma-deposited nitrogen-rich silicon nitride thin films," *J. Appl. Phys.* (submitted June 2005).
17. M. T. K. Soh, N. Savvides, P. J. Martin, and C. A. Musca, "On the bonding microstructure of amorphous silicon oxide thin films," *Thin Solid Films* (submitted April 2005).
18. R. M. Brody and V. J. Mazurczyk, *Semiconductors and Semimetals*, vol. 18, chap. 5 (Academic Press (New York), 1981).
19. D. K. Arch, R. A. Wood, and D. L. Smith, "High responsivity HgCdTe heterojunction photoconductor," *J. Appl. Phys.* **58**, 2360–70 (1985).
20. M. A. Kinch, S. R. Borrello, B. H. Breazeale, and A. Simmons, "Geometrical enhancement of HgCdTe photoconductive detectors," *Infrared Phys.* **17**, 137–45 (1977).
21. T. Ashley and C. T. Elliott, "Accumulation effects at contacts to *n*-type cadmium-mercury-telluride photoconductors," *Infrared Phys.* **22**, 367–76 (1982).
22. D. L. Smith, D. K. Arch, R. A. Wood, and M. W. Scott, "HgCdTe heterojunction contact photoconductor," *Appl. Phys. Lett.* **45**, 83–5 (1985).
23. J. F. Siliquini, C. A. Musca, B. D. Nener, and L. Faraone, "Temperature dependence of Hg_{0.68}Cd_{0.32}Te infrared photoconductor performance," *IEEE Trans. Electron Devices* **42**, 1441–8 (1995).
24. P. Capper, *Properties of Narrow Gap Cadmium-based Compounds*, chap. A6.2, pp. 212–4 (INSPEC (London, U.K.), 1994).
25. P. E. Petersen, *Semiconductors and Semimetals*, vol. 18, chap. 4 (Academic Press (New York), 1981).
26. R. L. Strong, J. D. Luttmmer, D. D. Little, T. H. Teherani, and C. R. Helms, "Characterization of anodic sulfide films on Hg_{0.78}Cd_{0.22}Te," *J. Vac. Sci. Technol. A, Vac. Surf. Films* **5**, 3207–10 (1987).
27. S. Adachi, *Optical Constants of Crystalline and Amorphous Semiconductors: numerical data and graphical information* (Springer, 1999).
28. F. L. Galeener, "Optical evidence for a network of cracklike voids in amorphous germanium," *Phys. Rev. Lett.* **27**, 1716–9 (1971).
29. E. D. Palik, ed., *Handbook of Optical Constants of Solids II* (Academic Press, Inc., 1991).

1. Introduction

The ability to observe and identify objects under adverse conditions, such as darkness and fog, is a highly desirable capability spanning a wide range of applications. Most of the infrared (IR) detector technology development has been sponsored by governments in an effort to enhance state security and provide battlefield superiority in conflict situations. Historically, active approaches such as illumination tools (torchlights, headlamps) have been employed to extend

operational capability into the night. However, the onset of the Cold War after 1945 saw the development of passive methods for reconnaissance and surveillance of perceived enemies. The passive approach involves the detection of ambient radiation reflected or radiated from the object of interest, with an emphasis on refining energy, spatial and temperature resolution [1].

Early IR detection science and technology was predominantly concerned with materials-related issues (performance, yield), and gradually evolved in complexity and sophistication with the development of micro-systems technology and associated micro-fabrication techniques [2]. Examples include focal-plane arrays [3, 4], micro-bolometers [5], micro-thermopiles [6] and micro-cantilever imaging systems [7, 8]. Nonetheless, such thermal heat sensing micro-systems are intrinsically broadband and disadvantaged by their slow response times in comparison to photonic detection systems based on semiconductors such as mercury cadmium telluride (HgCdTe). HgCdTe is very attractive as a detector material for IR imaging because one can alter its bandgap from 0.02 (HgTe) to 1.6 eV (CdTe) by varying its composition to cover the IR spectrum. The almost constant lattice spacing across the entire compositional range of the alloy also makes it possible to engineer the bandgap of the material during the growth phase. However, integration of HgCdTe detector technology with micro-fabrication technologies is hampered by the requirement to process the material at low temperatures (typically < 100 °C) in order to preserve its optical and electronic performance [9].

Whilst the mid-wavelength IR (3–5 μm) and long-wavelength IR (11–14 μm) continue to attract interest because of thermal imaging applications, the short-wavelength IR (SWIR: 1–3 μm) has significant appeal as a non-destructive diagnostic tool in a variety of process-automation domains including machine vision, astronomy, biomedicine, hot (1400 °C) metal processing, and as a quality control tool in the manufacture of optoelectronic devices (since silicon is ‘transparent’ in the SWIR).

Multispectral-imaging involves the photon energy discrimination of reflected or radiated radiation [10]. Currently, such systems typically weigh tens of kilograms and are relatively expensive [11, 12]. The present work intends to address the weight and size issues by reporting on the design, micro-fabrication, as well as the electronic and optical performance of an SWIR tuneable micro-filter prototype fabricated on HgCdTe. The compatibility of the micro-fabrication process with the HgCdTe material is evaluated by vacuum baking photoconductor structures at 125 °C for 1 hour, which is the approximate exposure time of the material to the highest process temperature step. Measurements of maximum responsivity and effective minority carrier lifetime pre- and post-bake indicate no effect. Uncooled operation of the device is preferable because the responsivity of the detector does not improve with thermo-electric cooling. This is due to the composition and doping of the HgCdTe. Optical measurements of tuneable micro-filter structures indicate wavelength tuning is possible between 1.7 μm and 2.2 μm using drive voltages up to 8 V, with the full-width-half-maximum (FWHM) of the resonance around 100 nm. Membrane deflection was up to 40% of the cavity width.

2. Micro-fabrication

A set of photoconductors was fabricated on *n*-type HgCdTe (DRS IR Technologies, Inc.) with cutoff wavelength (λ) around 2.6 μm . The process consisted of (a) mesa etching for the photoconductors, (b) insulator deposition and etching for metal contacts, and (c) chromium/gold metal deposition and liftoff (Fig. 1). Photoresist baking was done at 110 °C for no more than 3 minutes for each coating while the *a*-SiN_{*x*}H_{*y*} thin film insulating layer was deposited in 20 minutes by plasma-enhanced chemical-vapour deposition at 125 °C.

The micro-filters were fabricated on the photoconductors, with the process and qualitative results from unreleased devices reported previously [13]. Briefly, the process consisted of (a) bottom distributed Bragg reflector (DBR) deposition and polyimide (HD Microsystems) sacri-

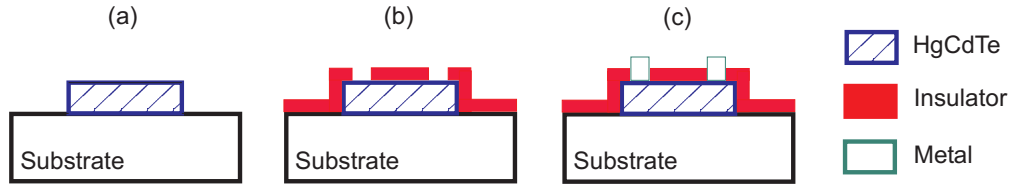


Fig. 1. Fabrication sequence of photoconductors: (a) mesa etching for the photoconductors, (b) insulator deposition and etching for metal contacts, and (c) metal deposition/lift-off.

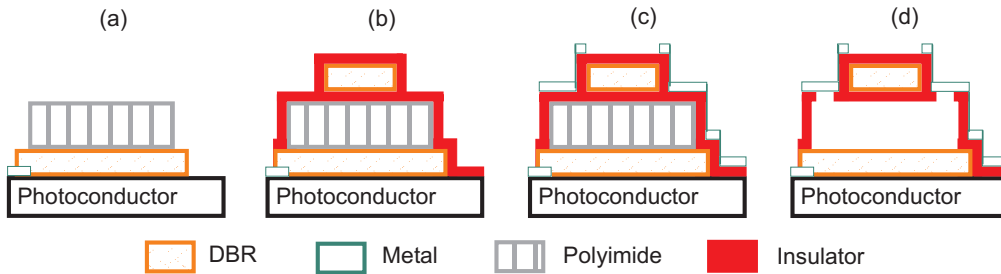


Fig. 2. Fabrication sequence of micro-filters: (a) bottom DBR deposition and polyimide sacrificial layer deposition, (b) deposition of $a\text{-SiN}_x\text{H}_y$ and top DBR, (c) metal deposition, and (d) membrane definition and release.

ficial layer spincoating and development, (b) deposition of $a\text{-SiN}_x\text{H}_y$ and top DBR, (c) metal deposition, and (d) membrane definition and release (Fig. 2). Each $a\text{-SiN}_x\text{H}_y$ deposition event was 20 minutes. The DBR consisted of an amorphous silicon oxide ($a\text{-SiO}_x$) thin film sandwiched between amorphous germanium ($a\text{-Ge}$) layers, both deposited in a thermal evaporator. Figure 3 illustrates the plan-view of the filter—note that the membrane arms are long to facilitate low-voltage actuation at the expense of fill-factor for this prototype. The engineering and management of thin-film strain and elastic properties were important considerations in the successful design and fabrication of the micro-filter. Investigations on the local bonding environment, thermal expansion behaviour, and elastic/plastic properties of the $a\text{-SiN}_x\text{H}_y$ thin films have been reported previously [14–16]. Varying the partial pressure of deposition was done to tune the residual strain of the $a\text{-SiO}_x$ films [17].

3. Measurement and calculation

3.1. Photoconductivity

The basic function of an electronic photodetector is to convert radiant input to an output that can be measured electronically. The responsivity \mathfrak{R} (VW^{-1}) of the detector is the ratio between the output signal and the radiant input:

$$\mathfrak{R}(\lambda) \equiv \frac{V(\lambda)}{P(\lambda)}, \quad (1)$$

where $V(\lambda)$ is the detector voltage (Volts) and $P(\lambda)$ is the incident radiant power (Watts).

The responsivity of a photoconductor is proportional to the applied electric field E (Vcm^{-1}). However, it has been observed to saturate for high bias voltages (V_b) due to the sweepout effect [18]. Briefly, recombination of photogenerated carriers may be enhanced at the contacts in a photoconductor by a high drift field. For high bias voltages, sweepout occurs when excess

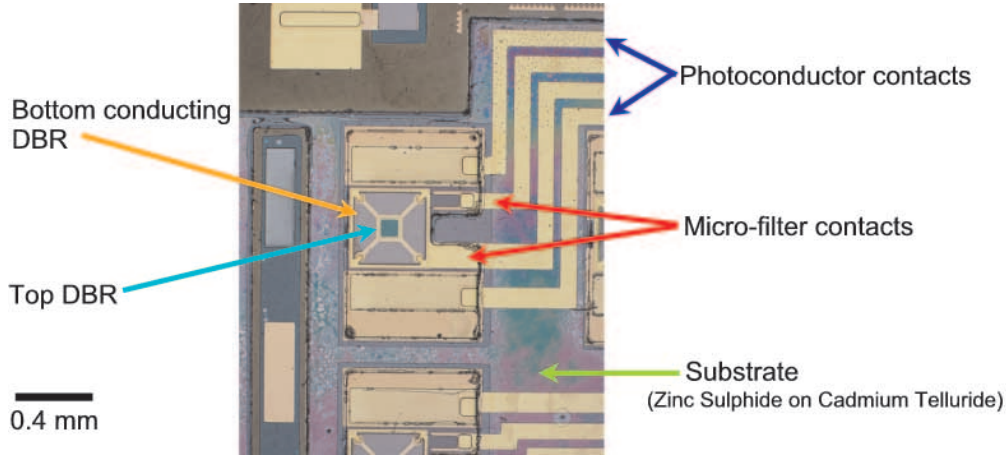


Fig. 3. Microscope image of a released (tuneable) micro-filter.

carriers are ‘swept’ toward the contacts and recombine. The responsivity will continue to increase with bias until all excess carriers are swept to the contacts, whereupon \mathfrak{R} saturates at a maximum value.

The effective lifetime τ_{eff} of photogenerated minority carriers may be used to quantify the performance of a photoconductor. τ_{eff} may be calculated from the responsivity equation which, for n -type material, is expressed as

$$\mathfrak{R}(\lambda) = \eta \frac{V_b \lambda}{hc} \frac{1}{wld} \frac{\tau_{eff}}{n_0}, \quad (2)$$

where η is the effective optical conversion efficiency, h ($= 6.626 \times 10^{-34} \text{ m}^2 \text{Kgs}^{-1}$) is Planck’s constant, c ($= 2.998 \times 10^8 \text{ ms}^{-1}$) is the speed of light, w ($= 400 \mu\text{m}$) is the device width, l ($= 400 \mu\text{m}$) is the device length, d ($= 7.1 \mu\text{m}$) is the HgCdTe epilayer thickness, and n_0 ($= 1 \times 10^{15} \text{ cm}^{-3}$) is the donor doping. τ_{eff} should have a V_b^{-1} relationship under sweep-out conditions [19]. Novel device architectures have been proposed to limit the sweepout effect in order to improve the performance of photoconductors [20–22], but were not implemented in the present work.

The responsivity provides no indication of the minimum radiant power that can be detected. This minimum radiant power is defined as the root-mean-square incident power required to produce an output signal equal to the detector noise level V_n , i.e. a signal-to-noise ratio of 1 divided by the noise equivalent power (NEP):

$$\text{NEP} \equiv \frac{V_n}{\mathfrak{R}(\lambda)}, \quad (3)$$

where the detectivity D is defined as the inverse of the NEP.

When the detectivity is employed to characterise a detector, it is necessary to specify the wavelength of the incident radiation, sampling frequency, bias applied (for photoconductors), detector area (wl), and detector operating temperature. D is not an ideal parameter for comparing detectors since it varies with detector area and frequency bandwidth [9]. Therefore, the specific detectivity D^* ($\text{cmHz}^{1/2} \text{ W}^{-1}$) has been introduced such that

$$D^* \equiv \frac{(wl\Delta f)^{1/2}}{\text{NEP}}, \quad (4)$$

which effectively gives the signal-to-noise ratio normalised to the detector area. Thermally-induced carrier generation-recombination noise limits the theoretical maximum specific detectivity at room temperature ($D_{thermal}^*$), and may be expressed as [23]:

$$D_{thermal}^* = \frac{\eta\lambda}{2hc} \left(\frac{\tau_{eff}}{n_0d} \right)^{1/2}. \quad (5)$$

Responsivity measurements of the HgCdTe photoconductors were performed using an Optonics Laboratories spectral response system as a function of wavelength ($1.8 \leq \lambda \leq 2.8 \mu\text{m}$) and at temperatures from 200 to 290 K. They were performed before and after a 1-hour vacuum oven bake at 125 °C in order to simulate the high temperature steps in the micro-filter fabrication process. The optical chopper frequency was set to 1 kHz (to minimise electronic noise) and the photoconductor active area was $1.6 \times 10^{-3} \text{ cm}^2$. The electric field applied was between 1.5 and 60 Vcm^{-1} . Noise measurements were performed on the devices housed in a specially-constructed grounded and shielded enclosure at 290 K.

3.2. Optical spectrometry

The optical design of a tuneable filter should optimise the resonance over the range of operation of photon energies. Optical resonance may be achieved through a Fabry-Pérot filter, which nominally consists of a set of two parallel highly reflecting mirrors separated by a displacement z_0 . Briefly, if photons of a particular wavelength are reflected inside the cavity in-phase, then constructive interference will result in a resonant transmission peak at that wavelength. Conversely, destructive interference will reduce transmission through the filter. The resonant wavelength is proportional to z_0 , and its full-width-half-maximum (FWHM) may be reduced by increasing the reflectance of the mirrors. However, in practice, metallic mirrors (which are highly reflective) are also absorbing in the IR. Therefore DBRs, which consist of transparent high and low refractive index materials in a ‘quarter-wave’ stack configuration, may be employed to address this issue.

Knowledge of the optical dispersion properties and deposition parameters (e.g. deposition rate) of the $a\text{-Ge}$, $a\text{-SiO}_x$ and $a\text{-SiN}_x\text{H}_y$ thin films used in the Fabry-Pérot configuration is required in order to design high performance DBRs. The optical constants of the thin films were extracted from reflection ellipsometry measurements between 2000 cm^{-1} and 6000 cm^{-1} ($1.8 \mu\text{m} - 5 \mu\text{m}$) [17]. Since the thin films are transparent over the photon energy range of operation, the refractive index (n) may be adequately modelled through the Cauchy parametric equation:

$$n(\lambda) = A + \frac{B}{\lambda^2}, \quad (6)$$

where A and B are the fitting parameters.

The spectral response of DBR test structures and tuneable micro-filters were measured using an in-house photometric set-up as illustrated in Fig. 4. A quartz-tungsten-halogen source provides the optical power which, after being monochromated, is focused onto the filter. The optical transmission of etalons fabricated on transparent substrates were measured using an external calibrated indium-gallium-arsenide detector (Judson Technologies, Inc.). Detector outputs were amplified and detected using a lock-in amplifier with the chopping signal of the light as a reference. Calculations using optical matrix models of materials (and their optical constants obtained from ellipsometry) in the optical devices were compared with measurements to extract information such as the DBR layer thicknesses, and membrane displacement (Δz) as a function of drive voltage (V_D).

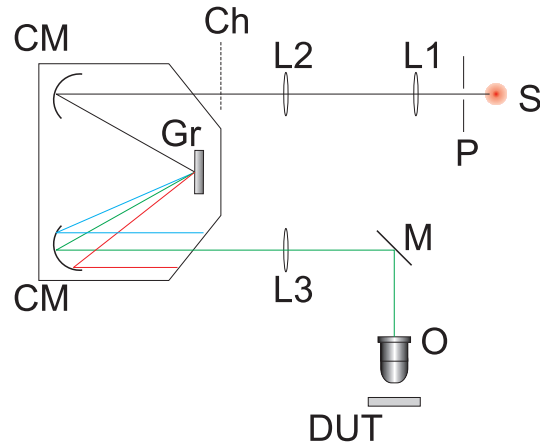


Fig. 4. Schematic of the spectrometric measurement setup. S: optical source; P: pinhole; L1-L3: lenses; Ch: chopper; CM: concave mirrors; Gr: diffraction grating; M: mirror; O: objective lens; DUT: device under test.

4. Results and discussion

4.1. Photoconductivity

Figures 5(a) and 5(b) plot typical responsivity and noise as a function of wavelength/frequency and V_b . Typical measurement uncertainty for responsivity was approximately 10%. Note that $\lambda = 2.4 \mu\text{m}$ roughly corresponds to the maximum responsivity of the devices for all measurement temperatures. From Fig. 6, it is evident that the photoconductor responsivity is independent of measurement temperature and heat treatment (baking). The intrinsic carrier concentration (n_i) in HgCdTe is dependent on temperature and, in particular, bandgap [24]. For temperatures $< 350 \text{ K}$, doping and material defects will influence device performance. It is well known that high temperature ($> 100 \text{ }^\circ\text{C}$) processing of HgCdTe may introduce defects that degrade device performance. However, this was not observed from the baking experiment of Fig. 6. These results indicate device performance is unaffected by room temperature operation, since cooling is not required to improve responsivity—thus reducing system cost and footprint.

Maximum effective lifetime and specific detectivity before and after baking was found to be $2 \times 10^{-5} \text{ s}$ and $8 \times 10^{10} \text{ cmHz}^{1/2}\text{W}^{-1}$, respectively (Fig. 7). Note that $\eta = 0.7$ (dewar window transmission) and noise measurements [Fig. 5(b)] were used in the calculation of τ_{eff} and D^* . Noise depends on frequency and applied bias. Briefly, the characteristic noise spectrum within a photoconductor consists of three components: Johnson noise, generation-recombination noise, and $1/f$ noise. Johnson noise is dependent on detector resistance, and is constant over a wide frequency range. Generation-recombination noise is related to fluctuations in the generation-recombination processes within a photoconductor, and rolls off at a corner frequency that is proportional to the effective lifetime. Finally, $1/f$ noise for photoconductors has a power spectrum that generally has a I/f dependence, where I is the current. The quadrature sum of these three components determines the minimum detectable signal of the photoconductor [18].

The effective lifetime was modelled using the method reported by Siliquini and co-workers [23]. Auger [25] and radiative [26] recombination process contributions were included, while Shockley-Read-Hall and surface recombination—which arise due to defects in the semiconductor crystal structure—were not considered. Measured τ_{eff} show a close match to theory for low bias voltages, with increasing deviation as the V_b increases. This is most likely due to

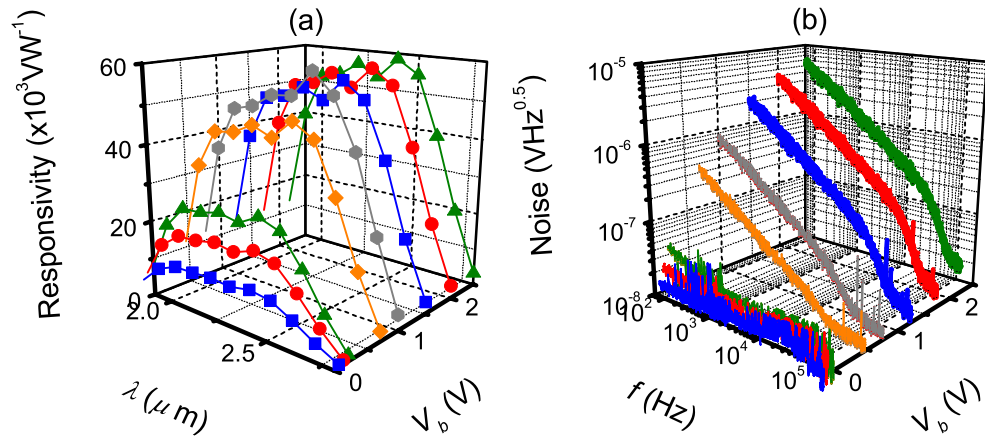


Fig. 5. (a) Photoconductor responsivity as a function of wavelength at $T = 290$ K, and (b) noise as a function of frequency. All measurements were taken at various voltage biases between 0.07 and 2.5 V.

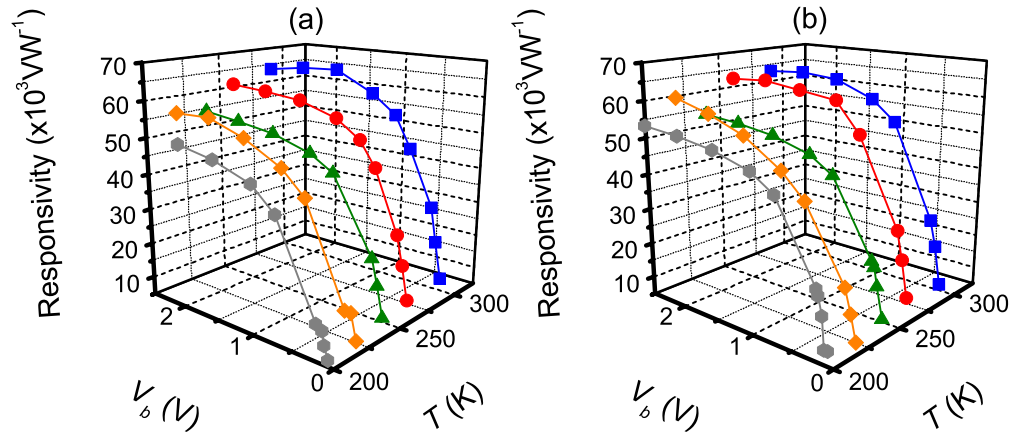


Fig. 6. Photoconductor responsivity at $\lambda = 2.4 \mu\text{m}$ as a function of measurement temperature and applied bias (a) before and (b) after a 1-hour bake at 125°C .

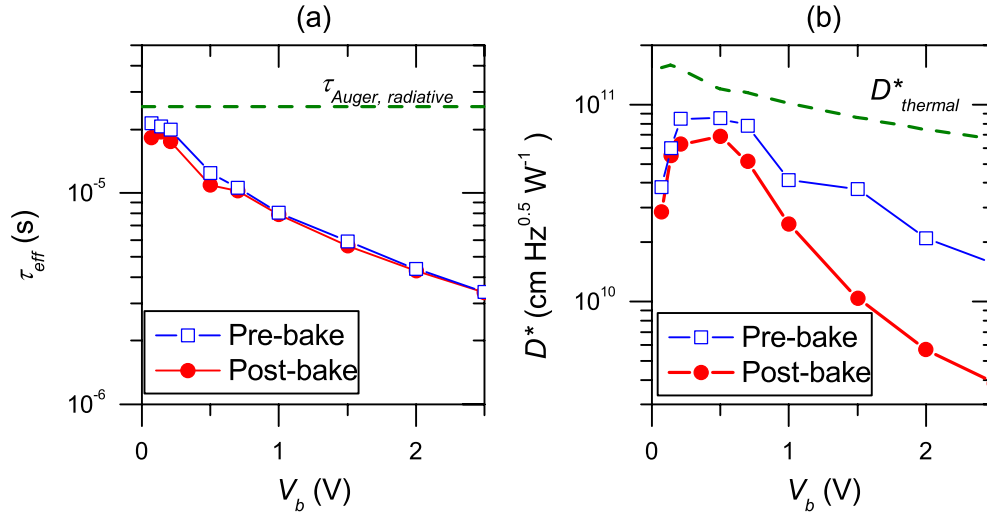


Fig. 7. Photoconductor (a) τ_{eff} and (b) D^* at $\lambda = 2.4 \mu\text{m}$ as a function of voltage bias at $T = 290 \text{ K}$. Shown alongside are the theoretical effective lifetime $\tau_{Auger, radiative}$ (taking into account Auger and radiative recombination processes) and $D^*_{thermal}$ [Eq. (5)], respectively.

sweepout effects [18]. The maximum specific detectivity [Fig. 7(a)] was calculated using the measured τ_{eff} . For $V_b > 0.5 \text{ V}$, D^* can be more than an order of magnitude lower than $D^*_{thermal}$. This may be due to the photoconductor no longer being limited by generation-recombination noise as the $1/f$ noise increases with increasing bias [Fig. 5(b)]. Furthermore, our experience is that the deterioration in the metal contact from acceptor (gold) diffusion induced by baking is responsible for a degradation in D^* at higher biases. Finally, the dominance of $1/f$ noise also corresponds to conditions under which sweepout effects are dominant. Additional analysis of the quantitative contributions of the various noise processes is required in order to understand the mechanisms that limit device performance.

4.2. Optical spectrometry

Figure 8 depicts the measured transmission of two fixed etalons with different cavity widths fabricated on a sapphire substrate, with calculated data for comparison. The filter structure and individual material optical constants and thicknesses are summarised in Table 1. {Note that the refractive index of the a -Ge layers is significantly lower than the tabulated values in the literature ($A \approx 4$) [27], and could be due to the presence of voids in the thin film morphology [28].} These two etalons were fabricated simultaneously for all steps of fabrication except for the polyimide deposition. Different thicknesses of polyimide were used to generate resonances at different wavelengths. Variations are observed in amplitude between the model and measurement because the model does not account for optical loss in the materials (e.g. optical gap absorption at lower wavelengths). However, there is good agreement between the model and measurement on the peak location and FWHM for both etalons.

The normalised spectral resonant response of a tuneable micro-filter fabricated on a HgCdTe photoconductor is presented in Fig. 9, and its optical structure is summarised in Table 2. Note that the measured a -Ge refractive index is lower than the Table 1 values due to the requirement to minimise strain-induced curvature in the top DBR after release. The inset in Fig. 9 shows a representation of the displacement motion of the filter, to scale vertically but, to allow rep-

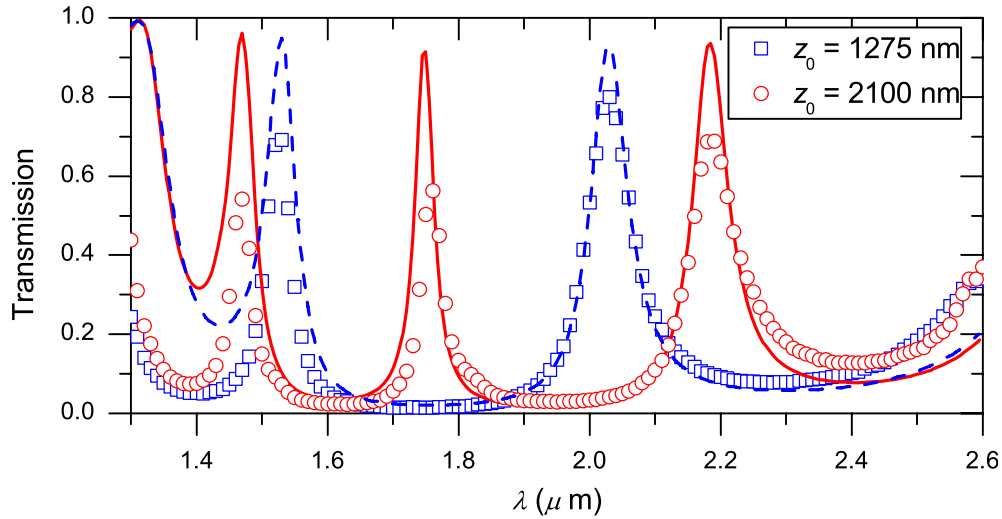


Fig. 8. Measured (points) and modelled (lines) transmission of two etalon test structures with varying cavity width. Amplitude deviations for $\lambda < 1.5 \mu\text{m}$ are caused by (optical gap) absorption, which was not included in the model.

Table 1. Fixed filter optical configuration including the Cauchy parameters for refractive index [Eq. (6)] and thickness of each material.

Filter	Material	Refractive index parameters		Thickness (nm)
		A	B	
Top DBR	<i>a</i> -Ge	2.81	0.18	145
	<i>a</i> -SiO _x	1.84	0.02	250
	<i>a</i> -Ge	2.81	0.18	145
Cavity	Polyimide	1.61	0.013	z_0
Bottom DBR	<i>a</i> -Ge	2.81	0.18	145
	<i>a</i> -SiO _x	1.84	0.02	250
	<i>a</i> -Ge	2.81	0.18	145
Substrate	Sapphire	Tabulated constants [29]		n/a

resentation here, not to scale laterally. The micro-filter demonstrates spectral tuneability from $2.2 \mu\text{m}$ to $1.7 \mu\text{m}$ for drive voltages up to 8 V. Relative membrane displacement and resonant FWHM vs drive voltage are plotted in Figs. 10(a) and 10(b), respectively. The results of Fig. 9 indicate membrane displacement up to 40% of z_0 and a FWHM of 100 nm throughout the tuning range.

5. Conclusion

The design, micro-fabrication, and electronic and optical performance of a SWIR micro-filter prototype was presented. The Fabry-Pérot micro-resonators were monolithically fabricated on HgCdTe, and consisted of two 3-layer *a*-Ge/*a*-SiO_x DBR stacks and *a*-SiN_xH_y encapsulation/mechanical layers deposited at 125 °C—the highest processing temperature. The total exposure time to that temperature was approximately 1 hour.

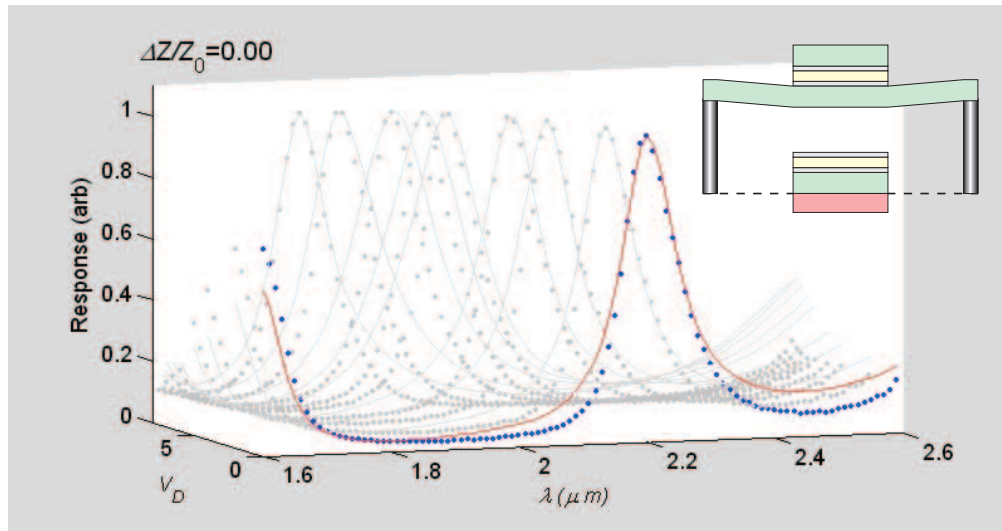


Fig. 9. Micro-filter spectral tuning characteristic for $1.7 < \lambda < 2.2 \mu\text{m}$ and $0 < V_D < 8.8 \text{ V}$. Δz is the membrane displacement. Each frame shows the theoretical response (solid line) using the optical model and parameters in Table 2, and the experimental measurements (dots). The inset shows a representation of the displacement motion of the filter, to scale vertically but, to allow representation here, not to scale laterally. *File size: 325 kB*

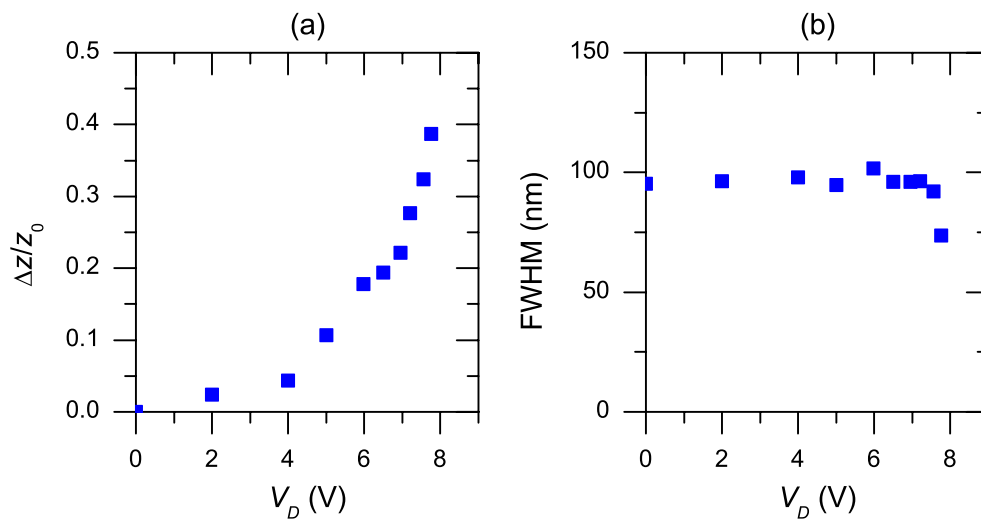


Fig. 10. (a) Micro-filter relative displacement and (b) FWHM of resonant peak vs drive voltage.

Table 2. Tuneable micro-filter optical configuration including the Cauchy parameters for refractive index [Eq. (6)] and thickness of each material.

Filter	Material	Refractive index parameters		Thickness (nm)
		A	B	
Top DBR	<i>a</i> -SiN _x H _y	1.72	0.008	570
	<i>a</i> -Ge	3.12	0.21	160
	<i>a</i> -SiO _x	1.84	0.02	290
	<i>a</i> -Ge	3.12	0.21	160
	<i>a</i> -SiN _x H _y	1.72	0.008	570
Cavity	Air	1	1	$z_0 = 1265$
Bottom DBR	<i>a</i> -Ge	3.12	0.21	160
	<i>a</i> -SiO _x	1.84	0.02	290
	<i>a</i> -Ge	3.12	0.21	160
Substrate	<i>a</i> -SiN _x H _y	1.72	0.008	570
	HgCdTe	n/a	n/a	n/a

Since high-temperature (> 100 °C) processing of HgCdTe may potentially degrade its electronic and optical performance, the impact of the 125 °C process was evaluated. Photoconductor structures were fabricated and baked at 125 °C in a vacuum-oven for an hour to simulate the thermal budget of the micro-filter fabrication process on the devices. Measurements of device responsivity as a function of wavelength ($1.9 \leq \lambda \leq 2.8$ μm) and temperature ($200 \leq T \leq 290$ K), effective minority carrier lifetime, noise and specific detectivity were observed to be unaffected by baking. Maximum responsivity, lifetime and specific detectivity were approximately 60×10^3 VW⁻¹, 2×10^{-5} s and 8×10^{10} cmHz^{1/2}W⁻¹, respectively. The maximum effective lifetime and specific detectivity are in reasonable agreement with the theoretical maxima. Uncooled operation of the device was preferable since the responsivity does not improve with thermo-electric cooling. This is due to the HgCdTe composition and doping.

Spectral tuning of the micro-filter was demonstrated between $1.7 < \lambda < 2.2$ μm for drive voltages up to 8 V, with FWHM around 100 nm throughout the tuning range. There was good agreement between the measured tuning response of the micro-filter and a filter model consisting of *a*-SiN_xH_y, *a*-Ge and *a*-SiO_x layers individually characterised (for refractive index and thickness) by FTIR ellipsometry. Membrane actuation for the tuneable micro-filters was up to 40% of the cavity width.

Acknowledgements

The authors are grateful to D. A. Scott of CSIRO Industrial Physics for objective comments and suggestions. M. Soh wishes to thank the Australian-American Fulbright Commission and Clough Engineering Ltd. for sponsoring his Research Fellowship in the United States. This work was financially supported by the Australian Research Council and CSIRO. HgCdTe material was supplied by P. Mitra, J. D. Beck and J. E. Robinson of DRS IR Technologies, Inc. under a DARPA program (Contract F33615-03-1-1421; Program Managers J. Carrano of DARPA and K. Barnard of AFRL).